HHS Public Access

Author manuscript

Med Phys. Author manuscript; available in PMC 2020 April 27.

Published in final edited form as:

Med Phys. 2018 November ; 45(11): 5030–5040. doi:10.1002/mp.13185.

Automatic localization of closely-spaced cochlear implant electrode arrays in clinical CTs

Yiyuan Zhao[a], **Benoit M. Dawant**[a], **Robert F. Labadie**[b], **Jack H. Noble**[a]

[a]Department of Electrical Engineering and Computer Science, Vanderbilt University, Nashville, TN 37235, USA

[b]Department of Otology – Head & Neck Surgery, Vanderbilt University, Nashville, TN 37235, USA

Abstract

Purpose: Cochlear Implants (CIs) are neural prosthetic devices that provide a sense of sound to people who experience profound hearing loss. Recent research has indicated that there is a significant correlation between hearing outcomes and the intra-cochlear locations of the electrodes. We have developed an image-guided cochlear implant programming (IGCIP) system based on this correlation to assist audiologists with programming CI devices. One crucial step in our IGCIP system is the localization of CI electrodes in post-implantation CTs. Existing methods for this step are either not fully automated or not robust. When the CI electrodes are closely-spaced, it is more difficult to identify individual electrodes because there is no intensity contrast between them in a clinical CT. The goal of this work is to automatically segment the closely-spaced CI electrode arrays in post-implantation clinical CTs.

Methods: The proposed method involves firstly identifying a bounding box that contains the cochlea by using a reference CT. Then, the intensity image and the vesselness response of the VOI are used to segment the regions of interest (ROIs) that may contain the electrode arrays. For each ROI, we apply a voxel thinning method to generate the medial axis line. We exhaustively search through all the possible connections of medial axis lines. For each possible connection, we define CI array centerline candidates by selecting two points on the connected medial axis lines as the array endpoints. For each CI array centerline candidate, we use a cost function to evaluate its quality, and the one with the lowest cost is selected as the array centerline. Then, we fit an *a-priori* known geometric model of the array to the centerline to localize the individual electrodes. The method was trained on 28 clinical CTs of CI recipients implanted with 3 models of closely-spaced CI arrays. The localization results are compared with the ground truth localization results manually generated by an expert.

Results: A validation study was conducted on 129 clinical CTs of CI recipients implanted with 3 models of closely-spaced arrays. 98% of the localization results generated by the proposed method had maximum localization errors lower than one voxel diagonal of the CTs. The mean localization

Corresponding Author: Yiyuan Zhao, Electrical Engineering and Computer Science, Vanderbilt University, 2301 Vanderbilt Pl., Nashville, TN 37235, **Work**: (615) 343-7798, yiyuan.zhao@vanderbilt.edu.

Disclosure of interest

The authors have no relevant conflicts of interest to disclose.

error was 0.13mm, which was close to the rater's consistency error (0.11mm). The method also outperformed the existing automatic electrode localization methods in our validation study.

Conclusion: Our validation study shows that our method can localize closely-spaced CI arrays with an accuracy close to what is achievable by an expert on clinical CTs. This represents a crucial step towards automating IGCIP and translating it from the laboratory to the clinical workflow.

Keywords

cochlear implant; electrode array; centerline localization; segmentation

1. Introduction

Cochlear implants (CIs) are neural prosthetic devices used for treating severe-to-profound hearing loss [1]. A CI device has a microphone, a processor, and a transmitter in the external component. The external component receives and processes sound signals and sends them to the internal component, which consists of an internal receiver coil and an electrode array implanted within the cochlea. The implanted CI electrodes receive the electrical signals delivered by the receiver coil, then stimulate the spiral ganglion (SG) nerves to induce a sense of hearing. The SG nerves are the nerve pathways that branch to the cochlea from the auditory nerves, which are tonotopically ordered by decreasing characteristic frequency along the length of the cochlea [2–3] (Shown in Figure 1). A SG nerve is stimulated if the frequency associated with it is present in the incoming sound [4]. During a CI surgery, a CI electrode array is blindly inserted into the cochlea by a surgeon. After the CI surgery, for each CI recipient, based on the hearing response, the audiologist adjusts stimulation levels for each individual electrode and selects a frequency allocation table to determine which electrodes should be activated when specific sound frequencies are detected. CIs lead to remarkable success in hearing restoration among the vast majority of recipients [5–6]. However, there are a significant number of users experiencing only marginal benefits.

Recent studies have demonstrated that there exists a correlation between hearing outcomes and the intra-cochlear locations of CI electrodes [7–12]. When multiple CI electrodes stimulate the same nerve pathways, those nerve pathways are activated in response to multiple frequency bands [13–14]. This is known as electrode interaction (or "competing stimulation"). Clinical studies conducted by our group have shown that hearing outcomes of CIs can be significantly improved by using an image-guided cochlear implant programming (IGCIP) technique we have designed [15]. In Figure 1 we show the CI electrodes activation patterns. With IGCIP techniques, we select an active electrode set in which the electrodes causing competing stimulations are identified and then deactivated [16–18]. To program the CI with IGCIP, we need to know the locations of the CI electrodes with respect to the intra-cochlear anatomy. However, CI placement is unique to each patient. Thus, identifying the intra-cochlear locations of CI electrodes for each individual CI recipient is a critical procedure in the IGCIP process.

Identifying the locations of the CI electrodes relative to intra-cochlear structure is difficult. First, segmenting the intra-cochlear structures is difficult because they are not visible in CT images. To solve this problem, we have proposed several methods that use a statistical shape

model to estimate the location of the invisible intra-cochlear anatomy by using the visible part of the external walls of the cochlea as landmarks [19–21]. Second, localizing CI electrodes in post-implantation CTs requires expertise. One challenge for localizing CI electrodes in clinical CTs is their limited resolution. The typical resolution of a clinical CT nowadays is on the order of $0.2 \times 0.2 \times 0.3\text{mm}^3$. Typical CI electrode size is around $0.3 \times 0.3 \times 0.1\text{mm}^3$, which is smaller than the size of a typical voxel. Thus, partial volume effects make it difficult to accurately localize CI electrodes, even with expertise. In a clinical CT, the voxels occupied by the metallic CI electrodes are assigned high intensity. For electrode arrays with electrodes pitched further than 1mm, the individual electrodes are separable thanks to the obvious intensity contrast between them. Thus, for localizing distantly-spaced CI electrode arrays, our group uses a graph-based method that relies on the intensity contrast between electrodes [22]. However, for arrays with electrodes spaced closer than 1mm, the method for localizing distantly-spaced electrode arrays does not generalize well because, as shown in Figure 2, there is typically no intensity contrast between them due to the lack of resolution and beam hardening artifacts. The second challenge is that there exist many FDA-approved closely-spaced CI electrode array models. The spacing of the electrodes on the array differs between models, which leads to different intensity features in the post-implantation CTs. Table 1 shows the three major types of closely-spaced electrode array models produced by Cochlear® (Sydney, New South Wales, Australia). Among the three types, CO1 and CO3 have electrode spacing distances that are lower than 0.8mm. In a clinical CT implanted with these two types of arrays, the voxels occupied by the electrodes are usually connected in a high intensity region, as shown in Figure 2c–d. CO2 has a relatively large electrode spacing distance compared to CO1 and CO3. In a clinical CT implanted with CO2, voxels occupied by those electrodes can be grouped into several regions, as shown in Figure 2a–b. The third challenge is the existence of false positive voxels. The wire lead and receiver coils are two sources of false positive voxels since they are also composed of metallic materials and have an appearance similar to the array in CTs. Another source of false positive voxels is the high density structures such as cortical bones. This is more common in a CT acquired with limited range of Hounsfield Unit (lCT). In a CT acquired with extended Hounsfield Unit (eCT), the intensity of the metallic material is much higher than the intensity of cortical bones, which makes the electrode array more separable from the cortical bones. In a lCT, the maximum intensity is limited to the intensity of cortical bones. Thus, the electrodes and the cortical bones are assigned the same maximum intensity, as shown in Figure 2c. All these three challenges complicate the automatic localization of closely-spaced electrode array in clinical CTs.

Braithwaite et al. and Bennink et al. have proposed two methods [23–24] directly related with electrode localization in CTs. Braithwaite et al. proposed a method [23] that uses a simple thresholding step followed by a specialized filter chain for distantly-spaced CI electrode arrays localization in CTs. This method relies on the intensity contrast between individual distantly-spaced electrodes. Thus, it cannot be directly applied to localizing closely-spaced electrode arrays due to the limited-to-no intensity contrast between individual contacts. This method is also not fully automated as human intervention is required for the initialization of the step used to connect the segmented electrodes in the correct order. Bennink et al. proposed a method [24] for localizing closely-spaced electrode arrays in CTs.

This method also requires a manual procedure to define a bounding box that includes all the electrodes to initialize the algorithm. It then uses an intensity profile matching algorithm to localize the individual electrodes on the initialized centerline extracted by a curve tracking algorithm. This intensity profile matching algorithm was designed and validated on a small set of lCTs, in which the voxels occupied by electrodes all have the same intensity value of 3071. In eCTs acquired by different scanners, the intensity values for individual electrodes are not homogeneous. The intensity profile matching algorithm would need to be modified for this method to be applicable to eCTs. Thus, the existing electrode localization methods cannot be directly adopted for fully automating IGCIP. In addition to the two aforementioned methods that are specifically designed for localizing electrodes in CTs, many methods exist for tubular structure segmentation. For instance, Cheng et al. presented a random walk-based curve tracking method for tubular structure segmentation in [25]. Feng et al. proposed a deformable model for tubular structure segmentation [26]. Li and Yezzi [27] developed a 4D minimal path algorithm for extraction of tubular structures. Manniesing et al. proposed a level set-based, topology-constrained surface evolution method [28] to iteratively localize the vessel axis of the tubular structure. A more thorough review of tubular segmentation methods is provided in [29]. Because the cochlear implant wire lead and electrodes form tubular structures, any general tubular shape localization method would need to be modified to separate the electrodes from the wire lead and estimate the position of each electrode.

In this work, we adopt a standard medial axis extraction based approach and customize it for fully automatic localization of closely-space electrode arrays in clinical CTs. We refer to the method as the “centerline-based” method (CL). The method is detailed in Section 2. We present the validation study of CL on a large-scale dataset of clinical CTs implanted with the three major types of closely-spaced CI arrays shown in Table 1. In our validation study, we compare CL with three existing methods developed by our group: (1) The Graph-based path-finding (GP) algorithm [22] for localizing distantly-spaced arrays, (2) Snake-based localization (SL) method [30] for localizing CO1, and a preliminary implementation of CL (pCL) [31]. In Sections 3 and 4, we present a quantitative comparison of the results generated by the three methods and discuss those results. In Section 5, we summarize the contributions of this work.

2. Methods

2.1. Dataset

Table 2 lists the dataset we use in this study. It consists of post-implantation clinical whole head CTs from 157 subjects acquired with different CT scanners. Manufacturers for the scanners used for acquiring CTs in our dataset include Xoran, Siemens, Philips, and GE. Among the 157 clinical CTs, 129 are eCTs and 28 are lCTs. Among the 129 eCTs in our dataset, 117 are acquired with a Xoran xCAT® from Vanderbilt University Medical Center. These Xoran eCTs have an isotropic voxel size. Among all the Xoran eCTs, 104 have voxel size $0.4 \times 0.4 \times 0.4\text{mm}^3$ (voxel diagonal 0.69mm) and 13 have voxel size $0.3 \times 0.3 \times 0.3\text{mm}^3$ (voxel diagonal 0.52mm). The remaining 12 eCTs are acquired by other scanners at other institutions with anisotropic voxels. There are 2, 4, and 6 that have a voxel diagonal

smaller than 0.50mm, 0.60mm, and 0.70mm, respectively. The 28 lCTs are all acquired at other institutions with CT scanners manufactured by Siemens, Philips, and GE. For these lCTs, the voxel sizes are all anisotropic and 16, 3, 3, 5, 1 of them have a voxel diagonal smaller than 0.50mm, 0.60mm, 0.70mm, 0.80mm, and 0.90mm, respectively. While most scanners available today are capable of producing eCTs, limited HU reconstructions are still the default setting at most centers. Our goal is for our method to be a general approach for both eCTs and lCTs to make it applicable to images that have already been acquired with limited Hounsfield Units or those that originate from centers where it is difficult to change current reconstruction protocols. Thus, in this study we have included both eCTs and lCTs in our dataset. Among the 157 CTs, the coarsest resolution is $0.37 \times 0.37 \times 0.63 mm^3$ (voxel diagonal 0.82mm).

We randomly selected 28 CTs as a training dataset for parameter tuning for our proposed CL method. The remaining 129 CTs were used for validation and they were not used in the training process. For each CT in our dataset, an expert manually localized the electrodes three times in all CTs. In each round, the expert manually localized the electrodes once in all the CTs and then started the next round after at least a one hour interval to avoid becoming familiar with any case. We randomly selected two sets out of the three manual localizations from the expert and averaged them to generate the ground truth localization results. The remaining set was used to compute the rater's consistency error (RCE), which is defined as the distance between the ground truth and the remaining localizations.

2.2. Method overview

The workflow of our proposed CL method is shown in Figure 3. The first step is to extract the volume of interest (VOI). The VOI is a sub-volume of the whole head CT that contains the cochlea and electrodes and is automatically estimated. Then, we compute a feature image which is the weighted sum of the intensity and the Frangi vesselness filter response [32] of the up-sampled VOI. We threshold the feature image to generate the regions of interest (ROIs), which are connected components in the thresholded feature image that contain electrodes or false positives. For each generated ROI, we perform a voxel thinning method [33] to generate its medial axis line. As is shown in Figure 3, the points on the actual centerline of the electrode array (shown in blue in Figure 3) are distributed across disconnected true positive ROIs. Meanwhile, there also exist several false positive ROIs that do not contain electrodes. When there are multiple ROIs, there exist many possible ways for connecting any number of their medial axes together. We refer to a given connection of medial axes as a "centerline candidate". Note that any centerline candidate constructed in this way cannot be treated as the array centerline directly because the endpoints of the centerline candidates do not always correspond to the two endpoints (the most basal and apical, as shown in Figure 1) electrodes on the array, for example, when the electrodes ROI also contains the lead as is shown in Figure 2d. Thus, we propose an approach to find an "array candidate" by exhaustively searching all the centerline candidates for the positions of the most basal and apical electrodes, such that the path formed by connecting the basal and apical electrodes along the centerline candidate optimizes a cost function we have designed. The pseudo-code for this algorithm is shown in Algorithm 1. The array candidate with minimum cost among all the centerline candidates found in the set of all possible

combinations of connections of the medial axis lines is selected as the centerline of the implanted array. Last, we resample the centerline of the implanted array by using the known electrode spacing distance of the array. The points on the resampled curve correspond to the centers of the electrodes. The following subsections present CL in details. All the parameters denoted with Greek letters are determined through a parameter tuning process in Section 3.1.

2.3. Medial axes generation

To extract the VOI from a whole head CT image, we register it to a reference CT where the VOI bounding box is known [34]. The reference CT is an "atlas" image where the position of the cochlea is known. Registration of the patient CT to the reference is used to define a bounding box containing the cochlea in the patient CT in a fully automatic fashion. All the subsequent procedures are performed on the VOI. We up-sample the VOI to a voxel size 0.1 × 0.1 × 0.1mm^3 so that the following voxel thinning method, described below, permits generating a finer resolution medial axis. The up-sampling process generates an up-sampled VOI with around 270 × 270 × 270 voxels. Next, we compute a feature image constructed as the weighted sum of the normalized intensity of image I and the normalized Frangi vesselness filter response I_V of the up-sampled VOI. The range of scales for the Frangi vesselness filter is selected as [0.5, 0.6]mm with a step of 0.05mm. The feature image is computed as:

$$I_f = (1-\rho)\frac{I - T_I(\alpha_I\%)}{T_I(\alpha_I\%)} + \rho\frac{I_V - T_V(\alpha_V\%)}{T_V(\alpha_V\%)} \quad (1)$$

where $T_I(\alpha_I\%)$, $T_V(\alpha_V\%)$ are functions which take percentage values $\alpha_I\%$ and $\alpha_V\%$ as inputs, and generate thresholds applied to I and I_V that correspond to the top $\alpha_I\%$ = 0.06% and $\alpha_V\%$ = 0.06% of the cumulative histogram of I and I_V, respectively. We include the vesselness filter response I_V in addition to the intensity I in I_f because it proved to effectively enhance the centerline of the electrode array in the previously developed snake-based localization method. ρ = 0.29 is a weighting scalar tuned for balancing the significance of I and I_V in Eqn. (1). After computing the feature image, we threshold it at 0 to generate ROIs, which are the connected components in the thresholded feature images containing electrode or false positives. After generating the ROIs, we perform a voxel thinning method [33] on each ROI to generate a medial axis line of the structure. The medial axis line consists of a set of ordered medial axis points. Those medial axis points are defined as the locus of locations which maximizes the Euclidean distance from the ROI's boundary.

2.4. Centerline localization and electrode localization

As mentioned in Section 2.2, array candidates are formed by evaluating all possible selections of basal and apical electrode position across the centerline candidates formed by all combinations of connections between ROIs. Since a centerline candidate is a set of medial axis points ordered on a curve, by selecting two different points and labeling them as apical and basal endpoints, we construct an array candidate by connecting the points on the curve between the two selected apical and basal endpoints. In a centerline candidate with n points, we can construct $n(n-1)$ different array candidates. An exhaustive search among all the possible array candidates is quick because (1) the maximum number of ROIs generated

by our proposed method is usually less than 4, and (2) a centerline candidate typically has $n < 200$ points. We exhaustively search all the array candidates and evaluate their quality by using a cost function defined as:

$$\text{Cost}(p) = \text{Cost}_\text{I}(p) + \text{Cost}_\text{S}(p) \tag{2}$$

where $\text{Cost}_\text{I}(p)$ is the intensity-based cost term for p, and $\text{Cost}_\text{S}(p)$ is the shape-based cost term for p. The cost function is designed to capture intensity and shape-based heuristics for a closely-spaced electrode array so that it returns a low cost for the actual centerline of the implanted electrode array and higher cost values for the other array candidates. First, the intensity-based cost term $\text{Cost}_\text{I}(p)$ evaluates a blob filter response at the selected most apical (a) and the selected most basal (b) (see Figure 1) endpoints:

$$\text{Cost}_\text{I}(p) = \frac{I_{B\max} - I_B(a)}{I_{B\max}} + \mu_1 \frac{I_{B\max} - I_B(b)}{I_{B\max}} \tag{3}$$

where $I_B(a)$ and $I_B(b)$ are blob filter responses for the selected apical and basal endpoints in an array candidate, respectively. $I_{B\max}$ is the maximum blob filter response among all the medial axis points. The blob filter response at voxel v is computed in a way that is similar to the Frangi vesselness filter [32] by using the three eigenvalues L_1, L_2, L_3 of the Heissian matrix computed at v:

$$I_b(v) = \begin{cases} B_1(v) \cdot B_2(v) \cdot B_3(v), & L_1, L_2, L_3 < 0 \\ 0, & \text{otherwise'} \end{cases} \tag{4}$$

The blob filter response is non-zero only when the three eigenvalues of the Hessian matrix at v are all negative. This is because the blob structures we detect are bright structures on a dark background. The three terms in Eqn. (4) are $B_1 = 1 - \exp\left(-\frac{\sum_{i=1}^{3} L_i^2}{S_1^2}\right)$, $B_2 = \exp\left(-\frac{r_{12} + r_{23} + r_{13}}{S_2}\right)$, and $B_3 = 1 - \exp\left(-\frac{L_{\min}}{S_3}\right)$, where $r_{ij} = |L_i - L_j|$, $L_{\min} = \min(-L_1, -L_2, -L_3$, $S_1 = T_I(a_I)$, $S_2 = 5000$, $S_3 = 40000$. Eqn. (3) captures the heuristic that we expect the voxels occupied by the endpoints to have a large blob filter response. Due to the fact that the electrodes are closely-spaced and the CT resolution is limited, there is a limited number of voxels with high blob filter response and the voxels occupied by the two endpoint electrodes are usually assigned high blob filter responses, as shown in Figure 3. Thus, we use the high blob filter response as an indicator to find the most apical and basal electrodes. We select the scales for the blob filter as the radius of the basal and apical electrodes in the brand of the implanted array. In Eqn. (3), we use $\mu_1 = 1.47$ as a weighting scalar to place extra emphasis on the blob response feature of the basal electrode compared to the apical electrode.

The shape-based cost function $\text{Cost}_\text{S}(p)$ captures geometric heuristics for the centerline of the implanted array. First, we define one hard constraint for constructing an array candidate with selected apical electrode (a) and basal electrode (b) as:

$$\mathrm{DOI}(a) > DOI(b) \tag{5}$$

In Eqn. (5), DOI(·) is the angular depth of insertion value. As the cochlea has a snail shape with 2.5 turns, the depth into the cochlea of any point can be quantified in terms of an angle from 0 to 900 degrees. To determine DOI(·), we use a segmentation of the cochlea. We segment the cochlea using automated techniques [19] in the pre-implantation CT when it is available and automatically register it to our target post-implantation CT. When a pre-implantation CT is not available, we segment the cochlea using automated techniques designed to segment the cochlea directly in the post-operative CT [20, 21]. In general, the apical electrode is inserted deeper into cochlea than the basal electrode. Thus, we only permit constructing an array candidate when the selected apical electrode has a larger depth of insertion value than the basal electrode. For array candidates satisfying Eqn. (5), we define the shape-based cost $\mathrm{Cost}_S(p)$ as:

$$\mathrm{Cost}_S(p) = \mu_2 \frac{\mathrm{DOI}(a)}{\mathrm{DOI}_{\max}} + |\|p\| - D_e| \begin{cases} \mu_3, & \mu_4 \le \dfrac{\|p\|}{D_e} \le 1 \\ \mu_3 + \mu_5\left(\mu_4 - \dfrac{\|p\|}{D_e}\right), & \dfrac{\|p\|}{D_e} < \mu_4 \\ \mu_3 + \mu_5\left(\dfrac{\|p\|}{D_e} - 1\right), & \dfrac{\|p\|}{D_e} > 1 \end{cases} \tag{6}$$

where $\mathrm{DOI}_{\max}$ is the maximum angular depth of insertion value among all the points on the initialized centerline. $\mu_2 = 8.89$, $\mu_3 = 0.27$, $\mu_4 = 0.9$, and $\mu_5 = 1.78$ are four tuned parameters. $\|p\|$ is the length of the array candidate p. D_e is the *a-priori* expected length of the array when it is straight, given by a 3D model of the implanted array. In the first term of Eqn. (6), we expect the apical electrode to have a large depth of insertion value. In the second term of Eqn. (6), we expect the length of the best array candidate to be close to the *a-priori* expected length. Since the array is not elastic, we should not expect the centerline of the implanted array to be longer than D_e. Curvature of the array can result in a small reduction of the centerline length. Thus, we design separate cost terms for centerlines with length falling within and outside a pre-defined length range. This pre-defined length range is empirically selected as [90%, 100%] of D_e. For array candidates with lengths out of the normal range, an extra cost weighted by μ_5 is added.

The centerline of the implanted array is determined as the array candidate that results in the lowest cost among all the centerline candidates. The resulting centerline is then resampled using the known *a-priori* electrode spacing distance of the array so that the points that form the resulting curve correspond to the centers of the electrodes to generate the final electrode array localization result.

2.5. Parameter selection process

The parameter selection process is performed with the 28 CTs in our training dataset. The initial values of those parameters are heuristically determined. Then, we sequentially and iteratively optimize each parameter until a local optimum is reached with respect to the

mean localization errors. After determining the parameter values, we use them to perform the validation study on the testing dataset.

2.6 Evaluation of methods

We implemented the automatic methods GP, pCL and CL in C++ on a standard Windows Server PC [Intel (R), Xeon (R) CPU X5570, 2.93GHz, 48GB Ram]. SL was implemented in Matlab on the same platform used for our previous study [30]. We applied GP, SL, pCL and our proposed CL methods to our testing dataset of 129 clinical CTs implanted with CO1, CO2, and CO3 arrays. GP and SL are two previously developed methods [22, 30] for localizing distantly-spaced electrode arrays and CO1 arrays, respectively. pCL [31] is a preliminary implementation of CL. To evaluate the accuracy of a localization result generated by an automatic electrode localization method, we compute the Euclidean distance between the positions found by the method and the corresponding ground truth positions. For each case, the mean localization error is computed by averaging the localization errors of all the electrodes on the array. As has been discussed in subsection 2.1, the rater's consistency error (RCE) is computed in the same way.

To detect differences between localization methods, we performed paired t-tests with Bonferroni correction on the mean localization errors generated by GP, SL, pCL, CL, and RCE on all the possible pairs independently. We visually confirmed that these datasets were reasonably well-approximated by a normal distribution to ensure a t-test was appropriate.

3. Results

3.1 Parameter tuning

Table 3 lists the parameter values selected after the parameter tuning process. To show the effectiveness of the parameters selected, we visualize the parameter sweeping procedure in Figure 4 with respect to the mean localization error in log-scale. Each parameter was swept from 0 to the double of its selected value with 11 uniform step sizes. The mean localization error for the training cases with the selected parameters is 0.11mm. As can be seen from Figure 4, all the parameters reached a local minimum in mean localization error at their selected values. Setting any parameter as 0 would lead to an increase of mean localization errors in the training dataset. This shows that all the terms in our design contribute to the accuracy of the localization results.

3.2. Validation study

The average running time for GP, SL, pCL, and CL from extracted VOI to electrode localization was ~8s, ~55s, ~40s, and ~42 seconds. Among the 129 testing cases, GP could not generate localization results for 52 cases. SL, pCL and CL could generate results for all the testing cases. The comparison of the mean/maximum electrode localization errors among GP (excluding the 52 cases for which GP cannot generate results), SL, pCL, CL, and RCE are shown as boxplots in Figure 5a. As can be seen from Figure 5a, CL generates localization results with a mean localization error of 0.13mm, which is close to the mean RCE (0.11mm). The three methods GP, SL and pCL have mean localization errors of 2.09mm, 2.06mm, and 0.94mm. In Figure 5b, we can see that CL generates 127 localization

results among 129 subjects (98%) that have maximum errors within one voxel diagonal, which is close to the RCE (100%) and outperforms the preliminary version pCL (80%) and the previously developed GP (5%) and SL (51%) methods. In Figure 6, we show two localization results generated by GP, SL, pCL and CL in comparison with the ground truth localization results for two cases with CTs of CI recipients implanted with a CO2 (Figure 6a) and a CO1 (Figure 6b) array. As we can see, the proposed CL method generates the most accurate automatic localization results compared with other existing methods.

The statistical t-test results of all the possible pairs of our automatic methods and the RCE are shown in Table 4. From the p-values, we find that our proposed method CL generates localization results that are significantly different from all the other methods and the RCE. However, the mean and maximum localization errors indicate CL can generate localization results with an accuracy that is close to the manual localization results generated by the CI electrode localization expert in our group.

4. Discussion

From the validation results presented in Section 3, we find 52 cases on which GP cannot generate valid results. This is because GP was designed for the localization of distantly-spaced arrays in CTs. One step in GP uses a voxel thinning method [33] to generate candidate nodes for the path-finding algorithms to find a fixed-length path with N candidate nodes (N is the number of the electrodes on the array). In the 52 cases, a path could not be found using the candidate nodes that has the length of the implanted array. From Figure 5, we find that the proposed CL method outperforms the existing automatic methods GP, SL, pCL, and CL. The two examples shown in Figure 6 also support this conclusion. In Figure 6a, we show an eCT implanted with a CO2 array. In this case, we cannot find a threshold that makes all the electrodes appear in a connected region with high intensity voxels. The threshold we select also includes the wire lead in the ROIs. GP generates inaccurate localization result by selecting two points on the wire lead as the two most basal electrodes. This is because the path-finding algorithm in GP cannot distinguish the voxels on the wire lead from the voxels occupied by electrodes. SL and pCL both ignore the electrodes that are not in the largest ROI. This is because both of the two methods assume all the electrodes are within one connected group of voxels with high intensity. CL successfully localizes all the electrodes by evaluating the array centerline candidates produced by all the possible connections of ROIs. Figure 6b shows results of a lCT implanted with a CO1 array. In this case, the voxels occupied by the wire lead and the electrodes have the same maximum intensity value. Thus, both GP and SL fail to distinguish the wire lead from the electrodes. To avoid localizing the voxels on the wire lead as the basal electrode, pCL added one process before endpoints selection. After generating the medial axis line of the largest connected region after thresholding the VOI, pCL performs an image erosion operation on the thresholded VOI with an empirically selected kernel size to eliminate the false positives on the wire lead before blob filter response computation for endpoints localization. Then, pCL constrains the search of the basal and apical electrodes within the remaining voxel groups (labeled with grey color). As can be seen in Figure 6b, the image erosion operation eliminates the voxel groups around the most basal electrode in this specific case. CL localizes the electrodes with a maximum error within one voxel diagonal in this case.

Without using image erosion for eliminating the false positives on the wire lead, CL uses the first cost term in Eqn. (6) to ensure that the points that are in the deeper region of the cochlea are more likely to be selected as the apical point. Then, with an optimal apical electrode selected, CL uses the second term in Eqn. (6) so that the selection of the basal electrode and the apical electrode forms an array candidate that has a length close to the implant model.

Even though CL has achieved accurate localization results on most of the CTs in our testing dataset, it still has several limitations. First, the initialization of the centerline of the electrode array is highly dependent on the intensity-based features. Any abnormal intensity-based features in the CTs may cause the mis-localization of the electrode array. Figure 7 shows two eCTs on which our proposed CL generates localization results with maximum localization errors larger than one voxel diagonal due to the abnormal intensity-based features. In Figure 7a, the voxels between the most basal electrode and the three most apical electrodes are assigned abnormally high intensity values. This causes CL to incorrectly localize the medial axis line, which further affects the centerline localization process. The automatically localized centerline deviates from the ground truth locations to the voxels that are closer to the apical end. In Figure 7b, the apical electrode is folded, which has been verified by an electrode localization expert (JN). However, the intensity feature does not show the folded electrode due to the limited resolution of clinical eCTs. Thus, CL mis-localizes the apical electrode and selects a false positive voxel on the wire lead as the basal electrode. The other existing methods all generate inaccurate localization results for these two cases. Failure cases as those shown in Figure 7 are rare, and our method generates accurate localization results on the remaining testing cases.

Another potential issue is that the locations of the electrodes between the apical and basal electrodes are determined by using a resampling method that relies on the *a-priori* known distances between individual electrodes. This process uses the apical and basal electrodes as landmarks and the accuracy of the electrodes in between them are only influenced by the accuracy of the localization of those two endpoint electrodes but not the local intensity-based features. An example of errors that can be improved can be seen in Figure 6a. In this example, the five most basal electrodes have obvious deviations from the center of the high intensity blob in the CT images. In this specific case, the CT has relatively high resolution and the electrodes have larger spacing distance between each other, some contrast between electrodes could be used in the electrode localization process to further improve the electrode localization accuracy. In future work, we will explore modifications to our approach to permit leveraging intensity contrast between electrodes when it is available.

Our proposed method uses a set of hand-crafted intensity-based and shape-based features inspired by expert heuristics. The determination of the parameters associated with all the hand-crafted features relies on a training procedure supervised by image processing experts. An alternative solution could be to rely on deep learning techniques. For instance, the ROIs could be generated using deep convolutional neural networks such as faster RCNN [35]. We are currently investigating these alternative approaches and will compare them to our current method.

The validation approach in our study can also be improved to further investigate the robustness of our proposed method. First, due to the limitation of our dataset, we do not have enough data to analyze the robustness of our method with respect to various acquisition parameters (the HU range, resolution, dose, and type of the implanted arrays) of the CTs and to electrode arrays model. In one of our previous studies [36], we use a cochlear phantom implanted with two models of distantly spaced CI arrays to perform a robustness analysis on the performance of a method for localization of distantly-spaced electrodes with respect to different dose levels, different HU ranges, different resolutions, and different models of CI electrode arrays. To evaluate the robustness of our proposed method with respect to these characteristics, we need to construct a new phantom implanted with closely-spaced CI electrode arrays. Another limitation of our validation approach is the accuracy of the ground truth. Our ground truth is based on clinical CTs with limited resolution, which introduces errors in the manual localization. To address this issue, we need to conduct a study similar to the one presented in [37] to better characterize the accuracy of our proposed method. This requires the acquisition μCT-CT pairs of cochlear specimens. The μCTs can be used to generate the ground truth since they have a higher resolution and our algorithm can be applied to the paired clinical CTs. The μCTs and CTs can then be registered, which would permit to analyze the electrode localization errors generated by our proposed method with a more a reliable ground truth.

5. Conclusion

Localization of CI electrode arrays is a crucial step to analyze electrode stimulation patterns in our IGCIP system. In clinical CTs implanted with closely-spaced electrode arrays, the identification of each individual electrode is difficult because the intensity contrast between electrodes is small. In this paper, we have proposed an automatic centerline-based method for the localization of closely-spaced CI electrode arrays in clinical CTs. The validation study shows that our method outperforms the existing methods for localizing CI electrodes. Our proposed method generates localization results with mean localization error of 0.13mm. 98% of our localization results have maximum localization errors lower than one voxel diagonal. These results show that our proposed method can generate localization results with errors that are close to the rater's consistency errors and are smaller than the errors produced by our earlier methods. It represents a crucial step in fully automating IGCIP and translating it from the laboratory to clinical use. It also enables us to conduct large-scale studies on electrode locations and their effect on hearing outcomes. Future work includes performing a robustness analysis on the proposed method by in a similar way as [36] so that we can determine the robustness of our proposed method with respect to different closely-spaced CI electrode array models and to a range of CT acquisition parameters. We also plan to perform a rigorous evaluation of the accuracy of our method by using highly accurate ground truth via μCTs [37] so that we can further analyze the impact of the errors in our electrode localization methods on the sensitivity of IGCIP.

Supplementary Material

Refer to Web version on PubMed Central for supplementary material.

Acknowledgement

This work was supported in part by grants R01DC014037 and R01DC014462 from the National Institute on Deafness and Other Communication Disorders. The content is solely the responsibility of the authors and does not necessarily represent the official views of these institutes.

Reference

[1]. National Institute on Deafness and Other Communication Disorders. NIDCD Fact Sheet: Cochlear Implants, 2016, NIH Publication No. 00-4798. https://www.nidcd.nih.gov/sites/default/files/Documents/health/hearing/FactsheetCochlearImplants.pdf Accessed March 30, 2018.

[2]. Greenwood DD. A cochlear frequency-position function for several species--29 years later. J. Acoust Soc Am. 1990; 87(6): 2592–2605. [PubMed: 2373794]

[3]. Stakhovskaya O, Sridhar D, Bonham BH, Leake PA. Frequency map for the human cochlear spiral ganglion: implications for cochlear implants. J Assoc Res Otolaryngol. 2007; 8(2): 220–233. [PubMed: 17318276]

[4]. Wilson BS, Dorman MF. Cochlear implants: current designs and future possibilities. J Rehabil Res Dev. 2008; 45(5): 695–730. [PubMed: 18816422]

[5]. Gifford RH, Hedley-Williams A, Spahr AJ. Clinical assessment of spectral modulation detection for adult cochlear implant recipients: a non-language based measure of performance outcomes Int J Audiol, 2014; 53(3): 159–164. [PubMed: 24456178]

[6]. Gifford RH, Shallop JK, Peterson AM. Speech recognition materials and ceiling effects: considerations for cochlear implant programs. Audiol Neurootol, 2008; 13(3): 193–205. [PubMed: 18212519]

[7]. Aschendorff A, Kubalek R, Turowski B, et al. Quality control after cochlear implant surgery by means of rotational tomography. Otol Neurotol, 2005; 26(1): 34–37. [PubMed: 15699717]

[8]. Rubinstein JT. How cochlear implants encode speech. Curr Opin Otolaryngol Head Neck Surg, 2004; 12(5): 444–448. [PubMed: 15377959]

[9]. Skinner MW, Holden TA, Whiting BR, et al. In vivo estimates of the position of advanced bionics electrode arrays in the human cochlea. Ann Otol Rhinol Laryngol Suppl, 2007; 197: 2–24. [PubMed: 17542465]

[10]. Verbist BM, Frijns JH, Geleijns J, Van Buchem MA. Multisection CT as a valuable tool in the postoperative assessment of cochlear implant patients. AJNR Am J Neuroradiol, 2005; 26(2): 424–429. [PubMed: 15709150]

[11]. Wanna GB, Noble JH, Carlson ML, et al. Impact of electrode design and surgical approach on scalar location and cochlear implant outcomes. Laryngoscope 2014; 124(Suppl 6): S1–S7.

[12]. Wanna GB, Noble JH, McRrackan TR, et al. Assessment of electrode placement and audiologic outcomes in bilateral cochlear implantation. Otol Neurotol, 2011; 32(3): 428–432. [PubMed: 21283037]

[13]. Boëx C, de Balthasar C, Kós MI, Pelizzone M. Electrical field interactions in different cochlear implant systems. J Acoust Soc Am, 2003; 114(4 pt 1): 2049–2057. [PubMed: 14587604]

[14]. Fu QJ., Nogaki G. Noise susceptibility of cochlear implant users: the role of spectral resolution and smearing. J Assoc Res Otolaryngol, 2005; 6(1): 19–27. [PubMed: 15735937]

[15]. Noble JH, Gifford RH, Hedley-Williams AJ, Dawant BM, Labadie RF. Clinical Evaluation of an Image-Guided Cochlear Implant Programming Strategy. Audiol Neurootol, 2014; 19(6): 400–411. [PubMed: 25402603]

[16]. Noble JH, Labadie RF, Gifford RH, Dawant BM, 2013. Image-guidance enables new methods for customizing cochlear implant stimulation strategies. IEEE Trans Neural Syst Rehabil Eng, 2013; 21(5): 820–829. [PubMed: 23529109]

[17]. Zhang D, Zhao Y, Noble JH, Dawant BM. Selecting electrode configurations for image-guided cochlear implant programming using template matching, J Med Imaging, 2014; 5(2): 021202.

[18]. Zhao Y, Dawant BM, and Noble JH. Automatic selection of the active electrode set for image-guided cochlear implant programming, J Med Imaging, 2016; 3(3): 035001.

[19]. Noble JH, Labadie RF, Majdani O, Dawant BM. Automatic Segmentation of Intra-Cochlear Anatomy in Conventional CT. IEEE Trans Biomed Eng. 2011; 58(9): 2625–2632. [PubMed: 21708495]

[20]. Reda FA, McRackan TR, Labadie RF, Dawant BM, Noble JH. Automatic segmentation of intra-cochlear anatomy in post-implantation CT of unilateral cochlear implant recipients. Med Image Anal. 2014; 18(3): 605–615. [PubMed: 24650801]

[21]. Reda FA, Noble JH, Labadie RF, Dawant BM. An artifact-robust, shape library-based algorithm for automatic segmentation of inner ear anatomy in post-cochlear-implantation CT. International Society for Optics and Photonics in SPIE Medical Imaging 2014.

[22]. Noble JH, Dawant BM. Automatic Graph-Based Localization of Cochlear Implant Electrodes in CT, In: Navab N, Hornegger J, Wells MW, Frangi FA (Eds.), Medical Image Computing and Computer-Assisted Intervention -- MICCAI 2015: 18th International Conference, 2015.

[23]. Braithwaite B, Kjer HM, Fagertun J, Ballaster MAG., Dhanasingh A, Mistrik P, Gerber N, Paulsen RR. Cochlear implant elecrode localization in post-operative CT using a spherical measure, 2016 IEEE 13th International Symposium on Biomedical Imaging (ISBI), 2016.

[24]. Bennink E, Peters JPM, Wendrich AW, Vonken E, van Zantan GA, Viergever MA. Automatic localization of cochlear implant electrode contacts in CT. Ear and Hearing, 2017; 38(6): e376–e384. [PubMed: 28379904]

[25]. Cheng J, Cole EB, Pisano ED, Shen D. Detection of Arterial Calcification in Mammograms by Random Walks. Inf Process Med Imaging. 2009; 21: 713–724 [PubMed: 19694306]

[26]. Wink O, Niessen W, Viergever M. Multiscale vessel tracking. IEEE Trans. Med. Imaging. 2004; 23(1): 130–133. [PubMed: 14719694]

[27]. Li H and Yezzi A Vessels as 4-D curves: global minimal 4-D paths to extract 3-D tubular surfaces and centerlines. IEEE Trans. Med. Imaging. 2007; 26(9): 1213–1223. [PubMed: 17896594]

[28]. Benmansour F, Cohen LD. A new interactive method for coronary arteries segmentation based on tubular anisotropy. In: Proc. IEEE Int. Symp. Biomed. Imaging, 2009.

[29]. Lesage D, Angelini E, Bloch I, Funka-Lea G. A review of 3D vessel lumen segmentation techniques: Models, features, and extraction schemes. Medical Image Analysis, 2009; 13(6): 819–845. [PubMed: 19818675]

[30]. Zhao Y, Dawant BM, Labadie RF, Noble JH. Automatic Localization of Cochlear Implant Electrodes in CT, In: Golland P, Hata N, Barillot C, Hornegger J, Howe R (Eds.), Medical Image Computing and Computer-Assisted Intervention -- MICCAI 2014: 17th International Conference, 2014

[31]. Zhao Y, Dawant BM, Noble JH. Automatic localization of cochlear implant electrodes in CTs with a limited intensity range. International Society for Optics and Photonics in SPIE Medical Imaging 2017.

[32]. Frangi AF, Niessen WJ, Vincken KL, Viergever MA. Multiscale vessel enhancement filtering, In: Wells WM, Colchester A, Delp S (Eds.), Medical Image Computing and Computer-Assisted Intervention -- MICCAI 1998: 1st International Conference, 1998.

[33]. Bouix S, Siddiqi K, Tannenbaum A. Flux driven automatic centerline extraction. Med Image Anal. 2005; 9(3): 209–221. [PubMed: 15854842]

[34]. Zhang D, Liu Y, Noble JH, Dawant BM. Localizing landmark sets in head CTs using random forests and a heuristic search algorithm for registration initialization. J Med Imaging. 2017; 4(4): 044007.

[35]. Ren S, He K, Girshick R, Sun J. Faster R-CNN: towards real-time object detection with region proposal networks. NIPS 2015 Proceedings of the 28th International Conference on Neural Information Processing Systems Volume 1: 91–99.

[36]. Chakravorti S, Bussey BJ, Zhao Y, Dawant BM, Labadie RF, Noble JH. Cochlear implant phantom for evaluating computed tomography acquisition parameters. J Med Imaging, 2017; 4(4): 045002

[37]. Zhao Y, Labadie RF, Dawant BM, Noble JH. Validation of cochlear implant electrode localization techniques, Proc. SPIE 10576, Medical Imaging 2018: Image-Guided Procedures, Robotic Interventions, and Modeling, 105761U.

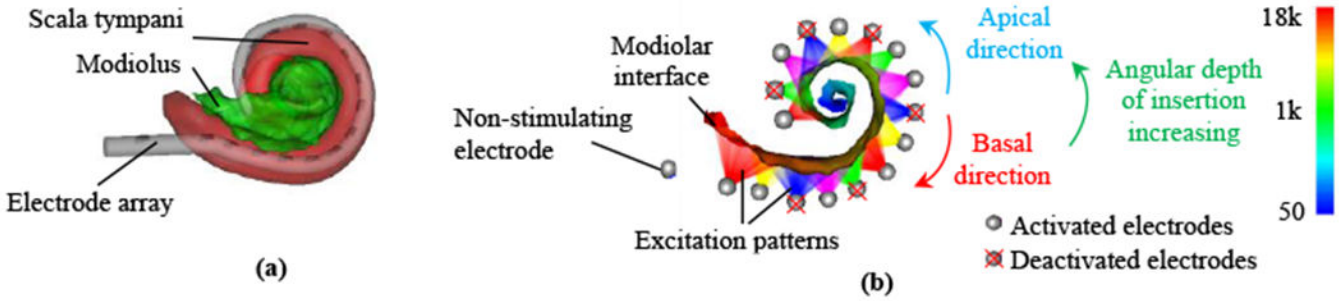

Figure 1.

Visualization of a CI electrode array and intra-cochlear anatomy after CI implantation surgery. In (a), the scala tympani (an intracochlear cavity) is shown with the modiolus, which represents the interface between the auditory nerves of the SG and the intra-cochlear cavities. In (b), a subject implanted with an Advanced Bionics 1J electrode array and stimulation patterns of the electrodes are shown. The modiolar surface is color-coded with tonotopic place frequencies of the SG in Hz.

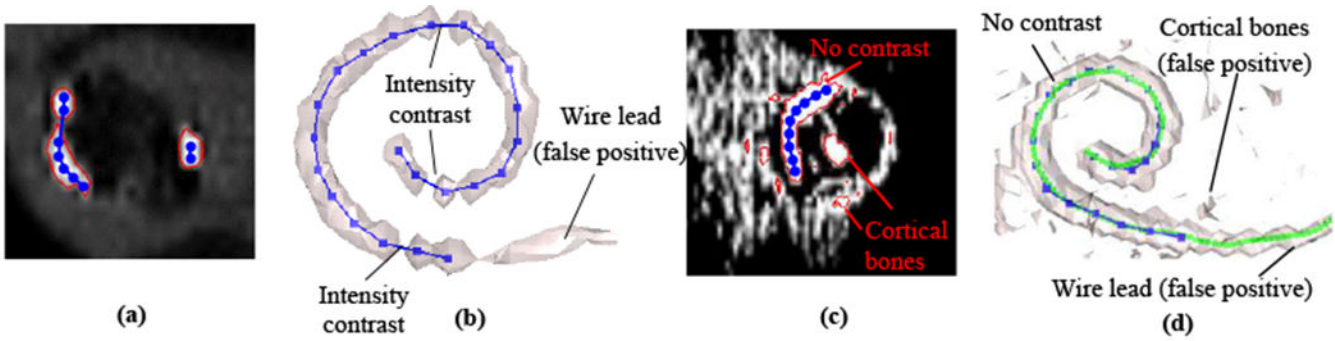

Figure 2.

Panel (a) and (c) show examples of two slices of CT in coronal view of recipients implanted with closely-spaced arrays. Blue points indicate the locations of individual electrodes. An iso-contour around high intensity voxels is shown in red. Panels (b) and (d) show 3D iso-surfaces of the electrode arrays with the manually determined electrode locations generated by an expert. In panel (d), we also show the medial axis line (in green) of the largest ROI extracted by our proposed method. As can be seen, the endpoints of the medial axis line do not always correspond to the electrodes on the two ends of the array.

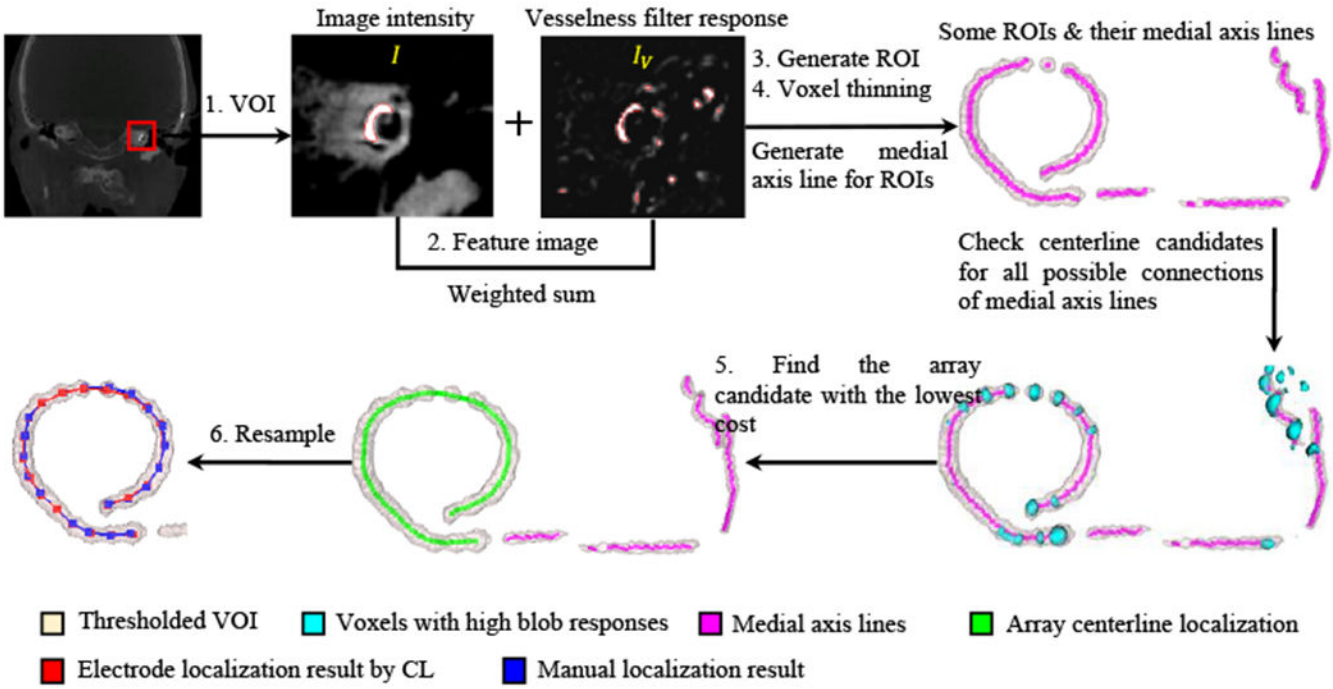

Figure 3.
Workflow of our proposed centerline-based method.

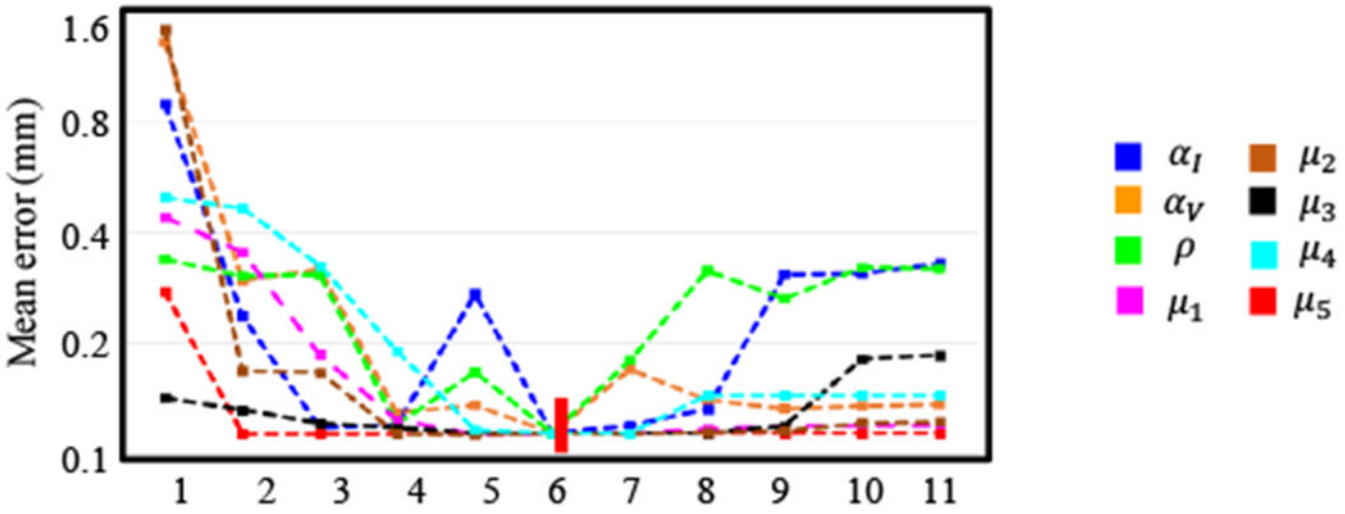

Figure 4.

The parameter tuning process for all the parameters in CL. The red hash mark indicates the finally selected parameter value.

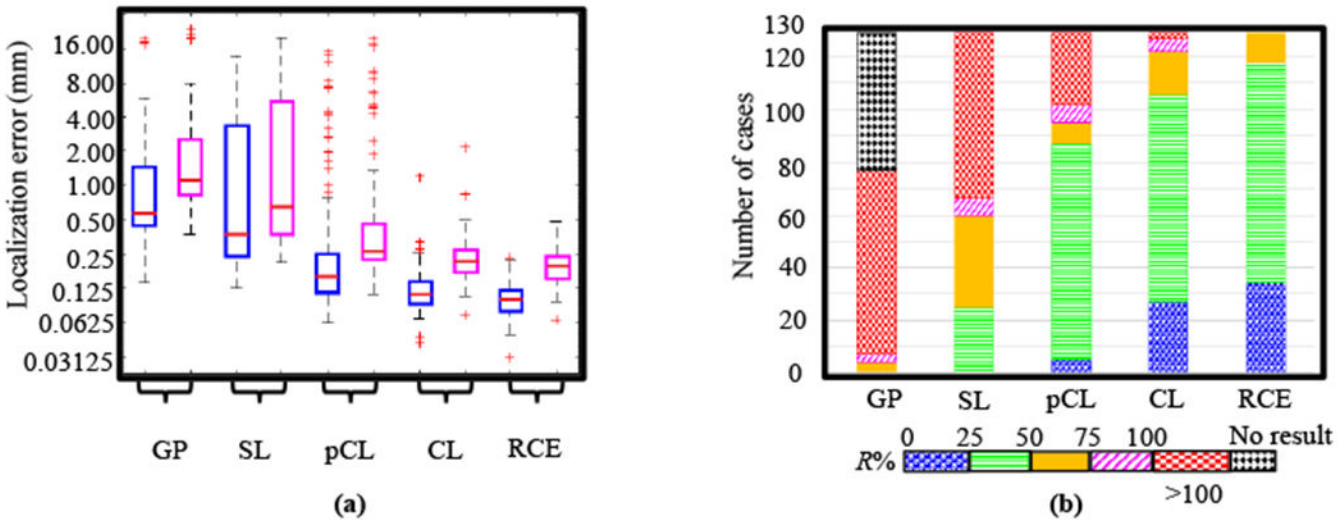

Figure 5.

Panel (a) shows the boxplots of mean (blue) and maximum (magenta) electrode localization errors in logscale among the different localization methods. Panel (b) shows the distribution of the ratio of the maximum localization errors with respect to the image voxel diagonal (*R* %) for different localization methods.

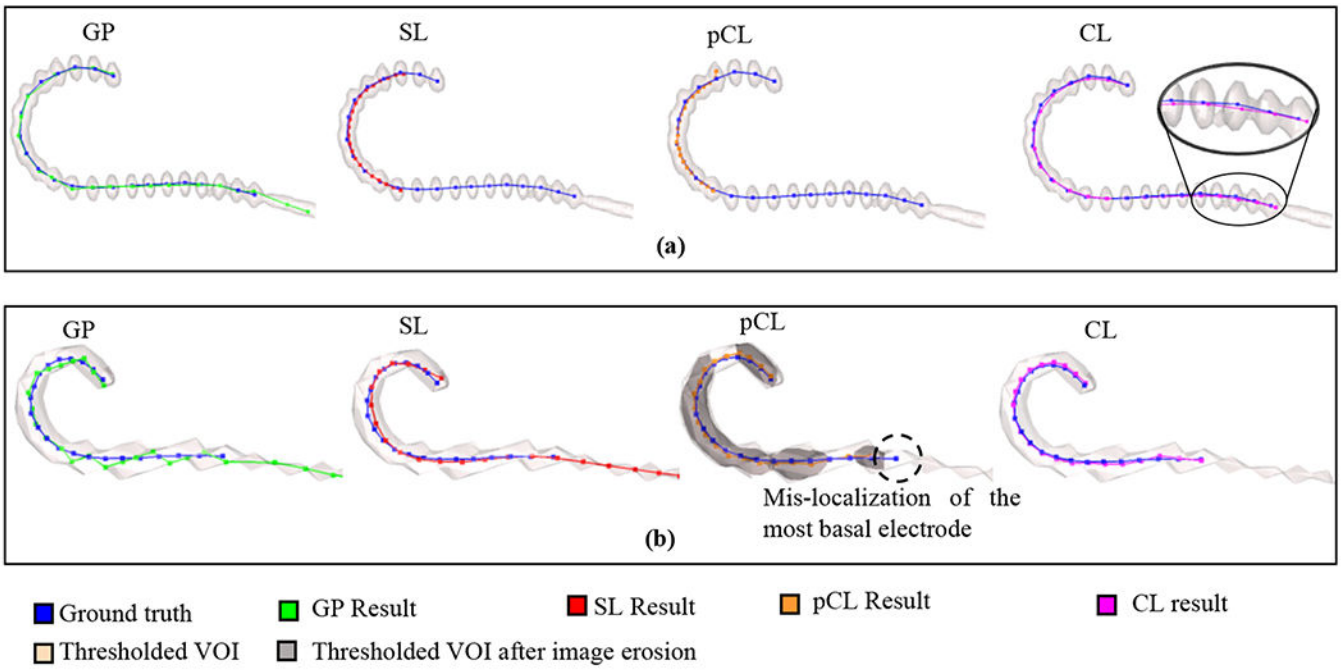

Figure 6.

Visualization of localization results generated by GP, SL, pCL, and CL in comparison with the manual ground truth localization results.

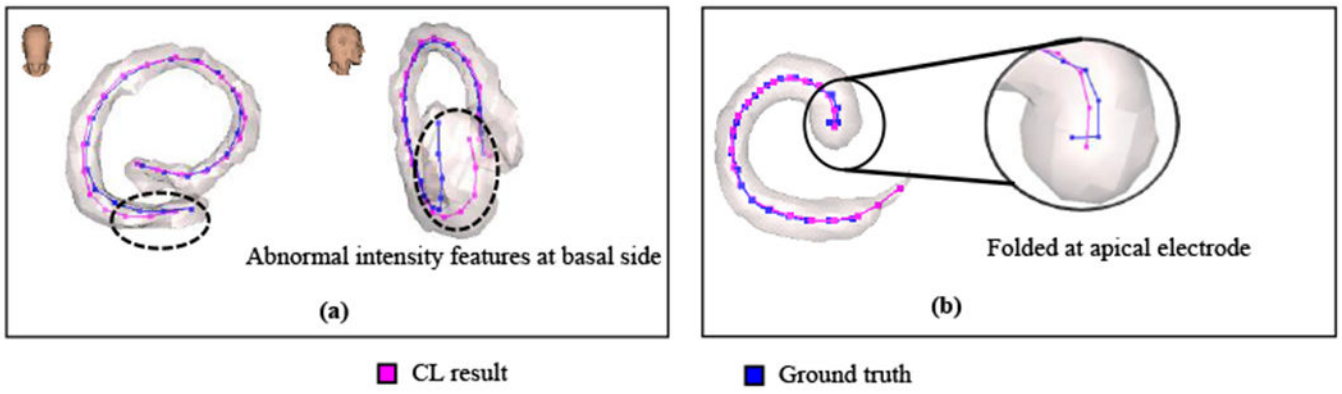

Figure 7.

Visualization of two eCT cases on which CL generates localization results with maximum errors larger than one voxel diagonal.

Table 1.

Specifications of different FDA-approved closely-spaced electrode arrays in our dataset

Electrode array brand	Total electrodes	Electrode spacing distance (mm)
Contour Advance (CO1)	22	~0.65
CI-422 (CO2)	22	~0.95
CI24RE-Straight (CO3)	32 (10 stiffening rings)	~0.75

Table 2.

Datasets used in this study

Purpose	Type of array	Number of eCTs	Number of lCTs	Total number of CTs
Training (28 CTs)	CO1	8	7	15
	CO2	8	2	10
	CO3	3	0	3
Validation (129 CTs)	CO1	78	10	88
	CO2	27	6	33
	CO3	5	3	8

Table 3.

The selected values for parameters in our proposed method

Parameters	Selected value	Parameters	Selected value
α_I(%)	0.06 (%)	μ_2	8.89
α_V(%)	0.06 (%)	μ_3	0.27
ρ	0.29	μ_4	0.90
μ_1	1.47	μ_5	1.78

Table 4.

P-value of the t-test results among mean localization errors by GP, SL, pCL, CL and RCE

	GP	SL	pCL	CL	RCE
GP	/	2.15×10^{-1}	2.16×10^{-1}	7.58×10^{-5}	6.81×10^{-5}
SL		/	1.03×10^{-4}	2.74×10^{-12}	1.42×10^{-12}
pCL			/	3.74×10^{-4}	2.44×10^{-4}
CL				/	6.30×10^{-3}
RCE					/